

# Single-Molecule Charge Transport through Positively Charged Electrostatic Anchors

Hongliang Chen,<sup>§</sup> Vitor Brasiliense,<sup>§</sup> Jingshan Mo, Long Zhang, Yang Jiao, Zhu Chen, Leighton O. Jones, Gen He, Qing-Hui Guo, Xiao-Yang Chen, Bo Song, George C. Schatz, and J. Fraser Stoddart\*



Cite This: *J. Am. Chem. Soc.* 2021, 143, 2886–2895



Read Online

ACCESS |



Metrics & More

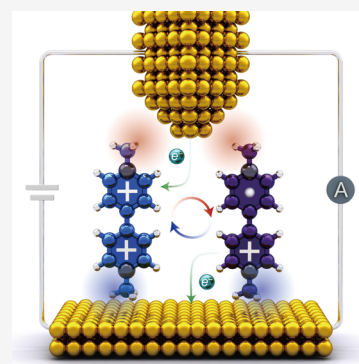


Article Recommendations



Supporting Information

**ABSTRACT:** The charge transport in single-molecule junctions depends critically on the chemical identity of the anchor groups that are used to connect the molecular wires to the electrodes. In this research, we report a new anchoring strategy, called the electrostatic anchor, formed through the efficient Coulombic interaction between the gold electrodes and the positively charged pyridinium terminal groups. Our results show that these pyridinium groups serve as efficient electrostatic anchors forming robust gold–molecule–gold junctions. We have also observed binary switching in dicationic viologen molecular junctions, demonstrating an electron injection-induced redox switching in single-molecule junctions. We attribute the difference in low- and high-conductance states to a dicationic ground state and a radical cationic metastable state, respectively. Overall, this anchoring strategy and redox-switching mechanism could constitute the basis for a new class of redox-activated single-molecule switches.



## INTRODUCTION

Advances in molecular electronics<sup>1</sup> during the past half century have enabled us to identify<sup>2–5</sup> hundreds of single-molecules that offer fundamental insight into the correlations<sup>6–11</sup> between molecular electronic structures and charge transport properties. Single-molecule junctions are generally constituted of a central conducting bridge, terminated<sup>8,9</sup> by anchors that are used to attach the molecular bridges to electrodes. From this perspective, an empirical rule-of-thumb for the design of single-molecules is that researchers should consider not only the electronic structure of the conducting bridges but also the chemical identity of the anchors and their binding behavior at the molecule/electrode interface.<sup>9,12</sup> On the basis of the nature of the binding interactions with the electrodes, anchors can be divided into three categories, namely, (i) dative anchors<sup>13–22</sup> (Figure 1a) which are bound to metal electrodes via coordinative interactions, (ii) supramolecular anchors<sup>23–26</sup> (Figure 1b) which couple to graphene electrodes through [ $\pi \cdots \pi$ ] interactions, and (iii) covalent anchors<sup>27–34</sup> (Figure 1c) which provide direct electrode–molecule contacts. The nature of these different binding interactions can be exploited in order to (i) improve<sup>33,35–37</sup> the stability and function of the connected conducting bridges, (ii) install<sup>38–40</sup> the current rectification in a junction, and (iii) modify<sup>41</sup> the dominant transport mechanism.

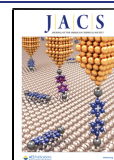
The electrostatic interactions between a molecule and the Au electrode have been observed to form stable Au–molecule–Au junctions in protonated pyrazolyl<sup>42</sup> and pyridinyl<sup>43</sup> anchors as well as in deprotonated imidazolyl<sup>44</sup> molecular junctions. In this work, we investigate systematically

the strategy of employing electrostatic interactions (Figure 1d) to form stable molecular junctions between the Au electrodes and positively charged methylpyridinium-terminated molecules. The conductance is measured using a home-built scanning tunneling microscope-based break junction (STM-BJ)<sup>13,45,46</sup> technique. By comparing the charge transport behavior of neutral pyridine-terminated and charged pyridinium-terminated single-molecule junctions, we have established that the electrostatic interaction can form stable connections to the Au electrodes in a similar manner as the lone electron pair does in dative anchors.

Such a binding strategy at the molecule/electrode interface, which we refer to here as electrostatic anchoring, also applies to many other backbones, showing that positively charged pyridinium units can serve as efficient anchors to form robust Au–molecule–Au junctions, resulting in conductive molecular bridges. In addition, we observe binary conductance states, namely, a dicationic ground state and a radical cationic metastable state, in the dimethyl viologen molecular junction. Combining the results from single-molecule experiments and electrochemical measurements, we ascribe the binary conductance signature to an electron injection/extraction-induced redox reaction in the junction, an attribution which differs

Received: December 5, 2020

Published: February 12, 2021



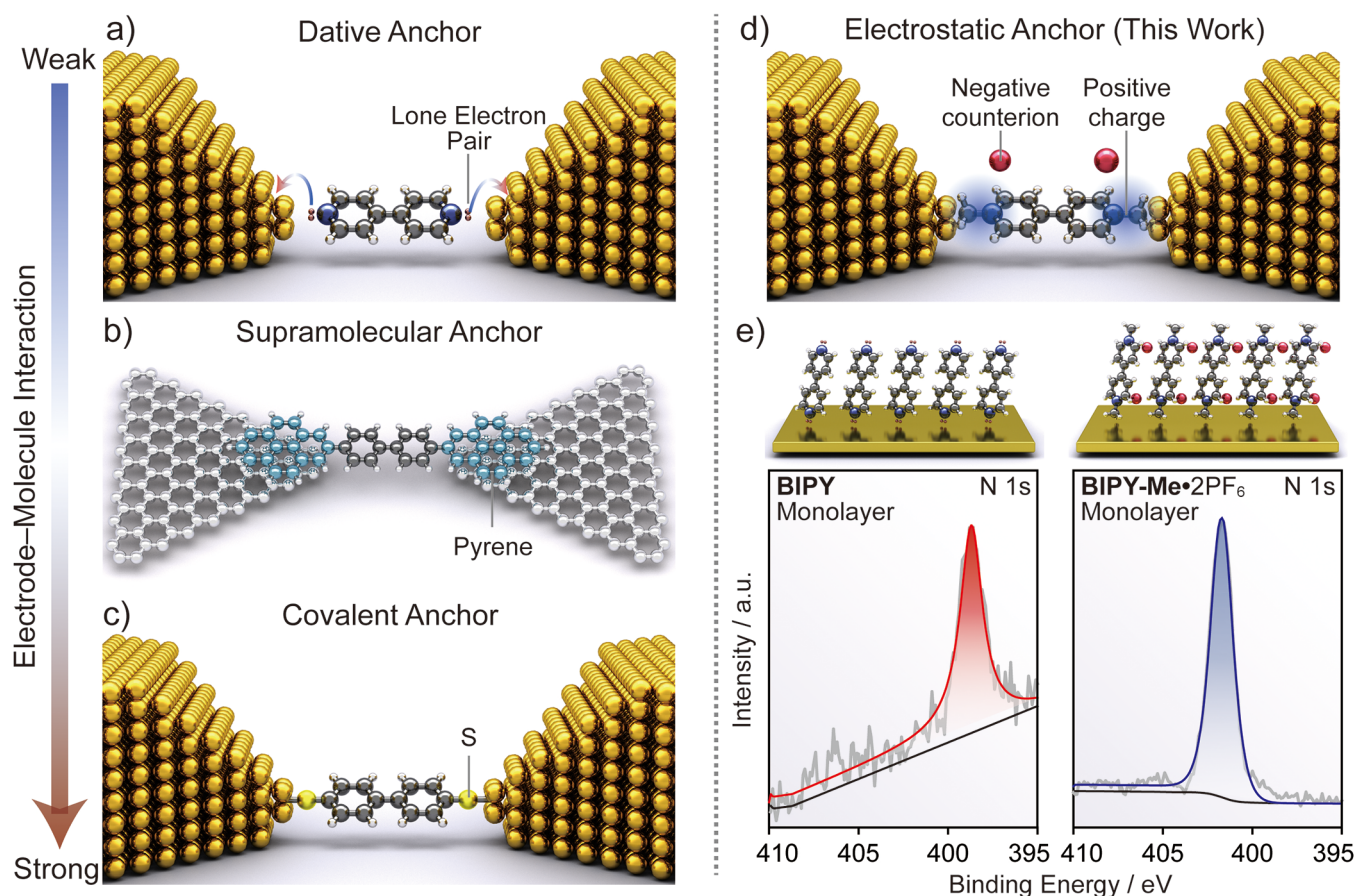


**Figure 1.** The development of an electrostatic anchor. Three widely used anchors employed in single-molecule junctions: (a) dative anchor, (b) supramolecular anchor, and (c) covalent anchor. (d) Electrostatic anchor developed in this work. (e) X-ray photoelectron spectra (XPS) showing different binding mechanisms for the monolayer of bipyridine (BIPY) (left) and the monolayer of dimethyl viologen (BIPY-Me<sup>2+</sup>) (right) adsorbed on Au substrates.

from the contact geometry-induced switching mechanism in pyridine-terminated molecular junctions.

We explore systematically the length-dependence and the role of counterions on the pyridinium-terminated molecular junctions. Our results show that oligophenylenes terminated with pyridinium anchors follow a quantum tunneling charge transport mechanism, with a molecular decay constant similar to that of pyridine-terminated analogues. We compare the remnant conductance signature of the N–N electrostatic anchor with that of the S–S dative anchor when they are present in very similar molecules. A three-level conductance feature has been demonstrated in these molecules with clear attribution to different contact conditions. These results establish our approach as a robust, yet flexible, strategy to distinguish the conductance states in positively charged molecular junctions<sup>43,47</sup> and macrocyclic circuits.<sup>48</sup> This work expands the library of chemical anchor groups and explores the intrinsic redox switching property in the viologen family of molecules, thereby opening up new opportunities for molecular electronics in the future.

## EXPERIMENTAL METHODS

**Synthesis.** The structural formulas and descriptors for all compounds used in the research reported in this paper are listed in Scheme S1. The pyridinium derivatives were prepared by microwave-assisted S<sub>N</sub>2 reactions at 90 °C. The full synthetic procedures and characterizations are outlined in the Supporting Information. See SI Sections A–C, Schemes S2–11, and Figures S1–20.

## X-ray Photoelectron Spectroscopy (XPS) Characterization.

XPS Analyses were carried out on thin films of 4,4'-bipyridine (BIPY) and methyl viologen (BIPY-Me•2PF<sub>6</sub>) obtained by spin-coating. The thickness and coverage can be tuned<sup>49</sup> by changing the speed of rotation from 3000 to 6000 rpm. XPS Depth analysis was performed by sputtering Ar ions on to the BIPY-Me•2PF<sub>6</sub> films.

**Electrochemical Experiments.** Cyclic voltammetry (CV) was carried out at room temperature in N<sub>2</sub>-purged MeCN with a Gamry Multipurpose instrument (Reference 600) interfaced to a computer. CVs on all samples (1 mM in MeCN) were performed using a glassy carbon working electrode (0.071 cm<sup>2</sup>), a Pt wire counter electrode, and a Ag/AgCl (3 M NaCl) reference electrode. Tetrabutylammonium hexafluorophosphate (TBAPF<sub>6</sub>) of 0.1 M concentration was used as the supporting electrolyte.

UV–vis spectro-electrochemical experiments were performed using a LAMBDA SYSTEM static experiment cuvette (1 mm optical path) with a Pt 80 mesh working electrode, a Pt wire counter electrode, and a Ag/AgCl (3 M NaCl) reference electrode. Compounds of 0.25 mM in MeCN were degassed using N<sub>2</sub> before being sealed in the cuvette. TBAPF<sub>6</sub> of 0.1 M was used as the supporting electrolyte. UV–vis Absorption spectra of BIPY-Me•2PF<sub>6</sub> at different potentials were recorded by applying a potential to the solution of BIPY-Me•2PF<sub>6</sub> for 1 min in a cuvette.

Electrochemical surface-enhanced Raman scattering (EC-SERS) spectra were recorded in a home-built cell setup with the target compounds (10 μM in H<sub>2</sub>O) adsorbed on AuFON SERS substrates. Substrates of Au film over nanospheres (AuFONs) were prepared according to a well-established procedure.<sup>50,51</sup> First, we cleaned a 25-mm silicon wafer (WaferNet Inc.) with a sequence including incubation in Piranha solution (H<sub>2</sub>SO<sub>4</sub>/H<sub>2</sub>O<sub>2</sub> = 3:1) and sonication

in H<sub>2</sub>O/H<sub>2</sub>O<sub>2</sub>/NH<sub>4</sub>OH (5:1:1). We then cleaned the substrates thoroughly with Milli-Q water, drop-cast a suspension of 300-nm SiO<sub>2</sub> microspheres (Bangs Laboratories, Inc.) onto the wafer, swirled them, and left them to dry under ambient conditions. Finally, a physical deposition system (PVD-75, Kurt J. Lesker) was used to deposit a 150-nm Au film at a rate of 0.5 Å s<sup>-1</sup> under low pressure (10<sup>-7</sup> Torr), forming the AuFONs substrates. The reference and counter electrodes used were Ag/AgCl (3 M NaCl) and Pt wires (99.99%, Alfa Aesar), respectively. The AuFONs substrate was employed as the working electrode. A potentiostat (EC301, Stanford Research Systems) was used to perform potential-step experiments in aerated or N<sub>2</sub>-saturated 0.1 M HClO<sub>4</sub>.

**STM-BJ Measurements.** Single-molecule conductances were measured using an STM-BJ,<sup>13,45,46</sup> housed inside a plastic glovebox filled with N<sub>2</sub>, with the target compounds dissolved (0.1 to 1 mM) in MeCN (Sigma-Aldrich, 99% purity). In order to suppress the background conductance of the solvent, an electrochemically etched Au tip (Ø = 0.25 mm, 99.999% purity, Alfa Aesar) was coated with Apiezon wax. The Au substrates were prepared by the evaporation of Au (99.999% purity, Alfa Aesar) at ~1 Å s<sup>-1</sup> to give 100-nm-thick Au on fresh silica (300 nm SiO<sub>2</sub>) substrates and were cleaned with Piranha solution before making measurements. During the STM-BJ experiments, 20 µL of the solution containing the test compounds was added to the substrate. Thousands of traces were collected and presented as one-dimensional (1D) and two-dimensional (2D) conductance-displacement histograms without data selection in order to obtain the most frequently observed conductance values. Further details are provided in SI Section F.

**Theoretical Methods.** The local electric field intensity and distribution in the nanogap between the tip and substrate in an STM were simulated using the AC/DC Module (steady state) of the COMSOL Multiphysics finite-element-analysis software (COMSOL Inc.). The molecular structures of BIPY-Me<sup>•+</sup> and BIPY-Me<sup>2+</sup> were optimized on a slab of two layers of Au(111), in the Spanish Initiative for Electronic Simulations with Thousands of Atoms (SIESTA, version 4.1-b3) program (PBE/DZP for CHN atoms, PBE/SZP for frozen Au atoms), using a k-grid size of 4 × 4 × 1 for the scattering region, a density matrix tolerance of 1.0 × 10<sup>-4</sup>, and a force tolerance of 0.05 eV Å<sup>-1</sup>. Another slab of Au was added to the other side of the molecule, and together with the former, constitutes the scattering region. One PF<sub>6</sub><sup>-</sup> anion was added to one BIPY-Me<sup>•+</sup> junction, and two PF<sub>6</sub><sup>-</sup> anions were added to BIPY-Me<sup>2+</sup> junction in order to form the radical cationic and dicationic molecular junctions, respectively. These junctions were optimized subsequently at the same theoretical level. The Green's functions were calculated individually for the left and right electrodes with six layers of Au(111) with each using the same level (k-grid size of 4 × 4 × 50 for the electrodes). The coordinates of these electrodes were added subsequently to each side of the scattering region and form the device junction collectively. The spin-polarized transport properties were computed with the Landau formalism following previous methods.<sup>52,53</sup> A spin of one unpaired electron was fixed in the BIPY-Me-PF<sub>6</sub> junction to simulate its monoradical nature. Further details are provided in SI Section E.

## RESULTS AND DISCUSSION

**Film Characterization.** In order to test the binding mechanisms of the pyridinium anchors on Au surfaces (Figure 1e), XPS characterization of monolayer samples on Au films, as well in powder samples, were recorded. BIPY was chosen as a reference compound. The XPS powder spectrum of BIPY exhibits (Figure S21a) a single peak at 397.9 eV, attributed to the pyridine-N. The deconvolution of the XPS spectrum of the BIPY monolayer also results (Figure 1e, bottom left and Figure S22) in a single peak that shows a binding energy displacement of 0.7 eV for the pyridine-N with respect to the corresponding peaks in the powder spectrum. This result is indicative of chemisorption of BIPY onto the Au surface by the lone electron pair on the pyridine-N atom. Similarly, the XPS

powder spectrum, registered for BIPY-Me-2PF<sub>6</sub>, can be fitted (Figure S21b) into a single peak at 401.4 eV, attributable to the positively charged pyridinium-N atom. The fitted XPS spectrum of the monolayer of BIPY-Me-2PF<sub>6</sub> results (Figure 1e, bottom right and Figure S23) in an intense peak at 401.7 eV. The 0.3-eV shift in energy between the powder sample and the monolayer confirms the existence of an electrostatic interaction between the dicationic BIPY-Me-2PF<sub>6</sub> and the Au substrate. We performed (Figure S24) a depth analysis on the BIPY-Me-2PF<sub>6</sub> film by removing the material slowly between each cycle of analysis without damaging the underlying BIPY-Me-2PF<sub>6</sub> film. Such depth-profiling XPS enables high-resolution chemical analysis of the molecules close to the electrodes. After sputtering with Ar ions for 1 s, the pyridinium-N 1s core-level spectrum of the BIPY-Me-2PF<sub>6</sub> film gave (Figure S24) two well-resolved peaks corresponding to the viologen radical-N<sup>•</sup> at 399.6 eV and the positively charged viologen-N<sup>+</sup> at 401.7 eV. With an extension of the sputtering time, no XPS peak was found for N<sup>+</sup>, suggesting an efficient reduction (Figures S25–S27) of dicationic BIPY-Me<sup>2+</sup> to radical cationic BIPY-Me<sup>•+</sup>.

**Single-Molecule Conductance Measurements.** In order to examine the electronic properties of pyridinium-terminated compounds, we performed single-molecule conductance measurements using the STM-BJ technique (SI Section F). Figure 2 shows logarithmically binned 1D and 2D single-molecule conductance-displacement histograms for three compounds, namely, neutral BIPY (Figure 2a), dicationic BIPY-Me<sup>2+</sup> (Figure 2e), and radical cationic BIPY-Me<sup>•+</sup> (Figure 2i). These 1D and 2D conductance histograms show peaks around integer multiples of G<sub>0</sub>, where G<sub>0</sub> = 2e<sup>2</sup>/h ≈ 77.5 µS is the conductance quantum, corresponding to Au–Au point contacts and more peaks below 1 G<sub>0</sub> corresponding to molecular junctions. The 1D conductance histogram (Figure 2b) shows two distinct conductance peaks for single BIPY junctions, corresponding to the most frequently observed conductance values, namely, a low-conductance (LC) state centered at ~10<sup>-3.9</sup> G<sub>0</sub> and a high-conductance (HC) state centered at ~10<sup>-3.3</sup> G<sub>0</sub>. The LC/HC bistable conductance signatures can be attributed<sup>54,55</sup> to the contact geometry change of the single-molecule junction during elongation, i.e., the HC state of the molecule resides at an angle between the Au electrodes, while in the LC state, the molecule is fully stretched out in the junction. The 2D conductance histogram also shows (Figure 2c) two well-distinguished conductance features with almost four times the difference in conductance between the HC and LC states. Moreover, we analyzed (Figure 2d) the correlation between these two kinds of conductance traces by compiling<sup>56,57</sup> the 2D covariance histogram. The significant correlation in the intersection of HC and LC states indicates that these two states occur sequentially in a single trace.

The single BIPY-Me<sup>2+</sup> junction (Figure 2e) also shows (Figure 2f and Figure S31) two well-separated peaks in the 1D conductance histograms, namely, a LC state centered at ~10<sup>-3.8</sup> G<sub>0</sub> and a HC state centered at ~10<sup>-2.0</sup> G<sub>0</sub>, that differ significantly from the conductance signature obtained for BIPY. The HC state of the BIPY-Me<sup>2+</sup> junction is much more conductive (×20) than the HC state of the BIPY junction: this observation indicates that the bistable conductance signatures for BIPY-Me<sup>2+</sup> cannot be attributed simply to the contact geometry change of the single-molecule junction during tip elongation. A 2D conductance histogram shows (Figure 2g and

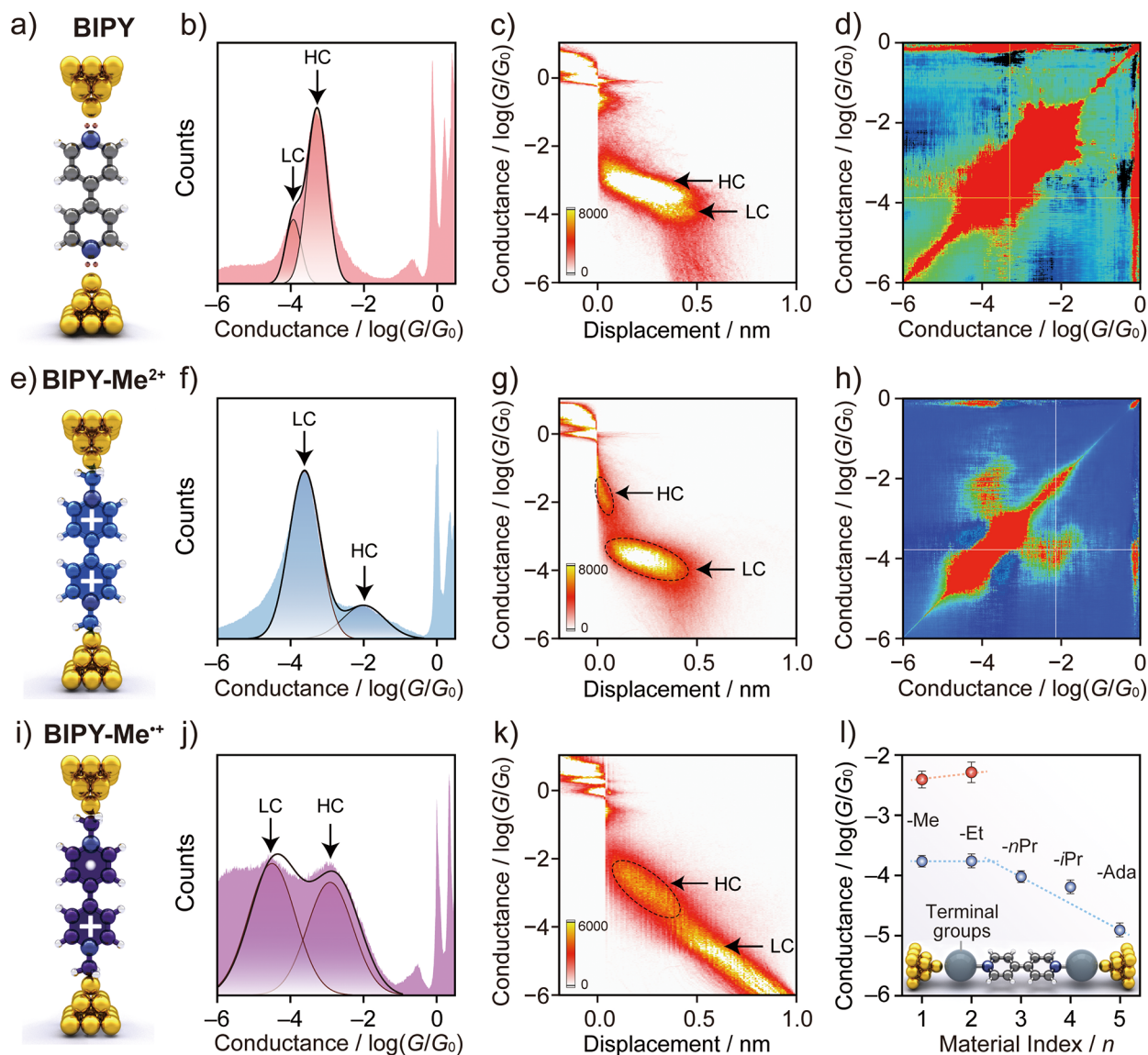


**Figure 2.** Electron transport of pyridine-terminated BIPY and pyridinium-terminated BIPY-Me<sup>2+</sup> molecular junctions. (a) Schematic of a single BIPY junction. (b) 1D and (c) 2D conductance–displacement histograms, and (d) 2D covariance histogram constructed from 3000 conductance–displacement traces, showing a bistable conductance signature. (e) Schematic of a single BIPY-Me<sup>2+</sup> junction. (f) 1D and (g) 2D conductance histograms, and (h) 2D covariance histogram constructed from 4100 conductance–displacement traces, also showing a bistable conductance signature. (i) Schematic of a single BIPY-Me<sup>+</sup> junction. (j) 1D and (k) 2D conductance histograms showing that the percentage of the HC state is increased significantly. (l) Conductance summary of viologens terminated with different terminal substituent groups on pyridinium rings.

Figure S31) an HC state starting (displacement =  $\sim 0.2$  Å) right after the break of the Au–Au point contact (displacement = 0), followed by a LC state (displacement = 0.2 to 0.5 nm), demonstrating two separate regions. Accounting for an Au–Au ‘snap-back’ distance<sup>28</sup> of  $0.5 \pm 0.1$  nm, the molecular length obtained from the relatively stretched distance distribution was determined to be  $\sim 0.7$  nm for the HC state and  $\sim 1.0$  nm for the LC state. We analyzed the correlation between these HC and LC traces by compiling<sup>56,57</sup> (Figure 2h) the 2D covariance histogram. Similar to the case of the BIPY junction, the more significant correlation in the intersection of the HC and LC states indicates that the molecular junction is constructed by these two states sequentially during each stretching cycle.

In order to confirm the original identity of the HC state, we performed a control experiment on the BIPY-Me<sup>+</sup> junction (prepared (Figure S27) by reducing the dicationic BIPY-Me<sup>2+</sup>

chemically with Zn dust in order to obtain its radical cationic state) and measured its conductance in an N<sub>2</sub>-filled glovebox. Radicals are believed to enhance<sup>58</sup> charge transport in single-molecule junctions on account of the increased transmission close to the SOMO orbital when the radicals are formed. In practice, the HC peak (Figure 2j) of the radical, centered on  $\sim 10^{-2.8} G_0$ , is similar in its magnitude to the HC value of the BIPY-Me<sup>2+</sup> junction. We have also obtained several differences in the conductance signatures of the BIPY-Me<sup>2+</sup> and BIPY-Me<sup>+</sup> junctions. First, the relative percentage of the HC state is larger in the BIPY-Me<sup>+</sup> junction for the simple reason that the starting material is a radical. Second, the displacement of the HC state for the BIPY-Me<sup>+</sup> junction is longer with a more pronounced slope compared with that for BIPY-Me<sup>2+</sup>. These differences can be explained by the formation<sup>59</sup> of a BIPY-Me<sup>+</sup> dimer in solution where one electrostatic anchor on each

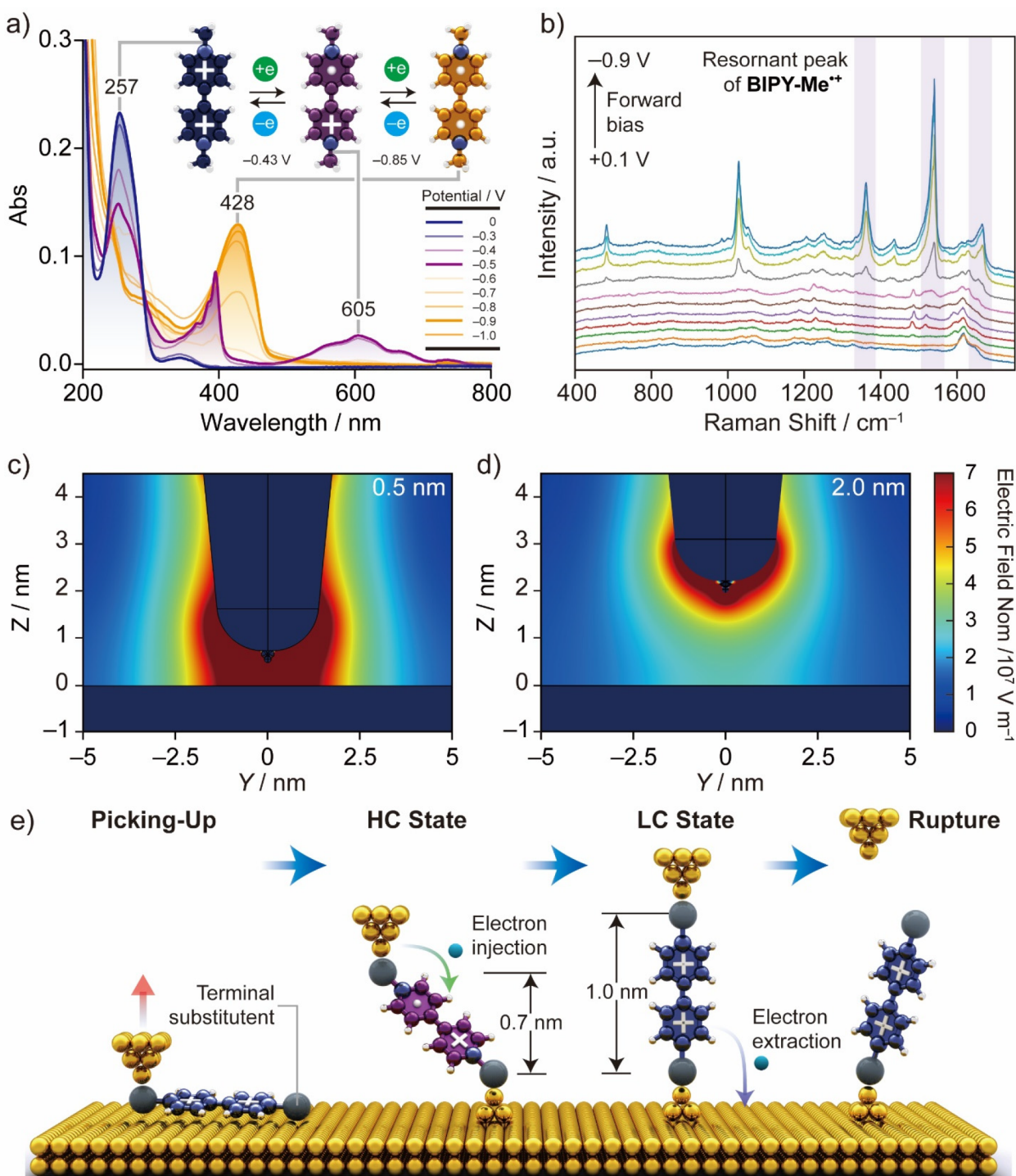


**Figure 3.** Electric-field-induced redox switching mechanism. (a) UV-vis Spectro-electrochemical measurements carried out on  $\text{BIPY-Me-2PF}_6$ . The UV-vis spectra recorded while applying a potential (vs Ag/AgCl) to the working electrode (Pt mesh) for 1 min. 0.1 M  $\text{TBAPF}_6$  in MeCN was employed as the supporting electrolyte. (b) Electrochemical Surface-Enhanced Raman Scattering (EC-SERS) spectroscopy carried out on  $\text{BIPY-Me-2Br}$  showing the formation of  $\text{BIPY-Me}^{2+}$  while applying forward bias (from +100 to  $-900$  mV with steps of  $-100$  mV) on an Au substrate. COMSOL simulation showing the spatial distribution of the electric field across the break junction with a gap of (c) 0.5 nm and (d) 2 nm between the STM tip and the substrate. (e) A plausible mechanism for the electron injection-induced redox switching mechanism in the single-molecule junction during elongation.

molecule binds to the Au electrode and the conduction occurs through the  $\pi$ - $\pi$  conjugation associated with the two viologen radical backbones. Qualitatively, a comparison of the 2D histograms, illustrated in Figure 2c,g,k, suggests that in the  $\text{BIPY-Me}^{2+}$  junction, the HC state with a short displacement

behaves like a radical species of  $\text{BIPY-Me}^{2+}$ , while the LC state with a fully stretched conformation corresponds to the oxidized  $\text{BIPY-Me}^{2+}$ . These results were supported by spin-polarized non-equilibrium Green's functions density functional theory (NEGF-DFT) calculations (Figure S28 and

Table S1), which reproduces the same trend, namely, the HC state being the  $\text{BIPY-Me}^{\bullet+}$  and the LC state being the  $\text{BIPY-Me}^{2+}$ . We hypothesize that an *in situ* redox reaction is taking place in the junction by the electric-field-induced electron injection/extraction to/from the single molecule.

**Redox Switching Mechanism.** We investigated the hypothesis of electric-field induced redox reactions by relying on spectro-electrochemical experiments to measure the required driving force for carrying out the reduction from  $\text{BIPY-Me}^{2+}$  to  $\text{BIPY-Me}^{\bullet+}$ . Figure 3a shows the *in situ* formation of  $\text{BIPY-Me}^{\bullet+}$  under potentiostatic control by UV-vis spectro-electrochemistry. At low potentials, we observe a band at 257 nm, characteristic of the HOMO-LUMO transition of  $\text{BIPY-Me}^{2+}$ . At about  $-400$  mV, the starting dication begins to be converted to the radical cationic  $\text{BIPY-Me}^{\bullet+}$ , as supported by the presence of isosbestic points at 250 and 300 nm as well as new peaks which arise at 398 and 605 nm for  $\text{BIPY-Me}^{\bullet+}$ . These conclusions are corroborated (Figure 3b) by EC-SERS. As the potential is lowered beyond  $-400$  mV, characteristic bands appear at 1350, 1530, and 1665  $\text{cm}^{-1}$  for  $\text{BIPY-Me}^{\bullet+}$ , accompanied by an increase in intensity of these peaks on account of the resonance of the radical species with the excitation wavelength, namely  $\lambda = 633$  nm.

$\text{BIPY-Me}^{2+}$  is usually employed<sup>60–62</sup> as a probe molecule to determine the quantum yield of electron transfer between excited Au clusters and  $\text{BIPY-Me}^{2+}$  in aqueous solution. Break-junctions with very small distances ( $<2$  nm) between the metal tip and substrate appear to facilitate the electron transfer which can be attributed<sup>63–65</sup> to the strong electric field ( $\sim 3 \times 10^8$  V  $\text{m}^{-1}$ ) formed (Figure 3c,d) when a small bias (100 mV) is imposed at small distances. In order to reveal the role of electric fields on electron catalysis, we simulated (SI Section E) the electric field distribution in the break-junction using an AC/DC Module (steady state) of COMSOL. The simulation was performed (Figure S29) using a 3D model with the electrical field generated between a top and bottom electrode in order to evaluate the focus of the localized electrical field in STM-BJs. The results of the simulation (Figure S30) reveal that the electrical field was focused on the end of the top electrodes and decreased rapidly during tip elongation. The intensity measured in the middle of the junction with a 0.5- and 2-nm gap size differs by almost a factor of 10. We are led, therefore, to propose that, only in the case when a molecule is trapped in the junction with a small gap size and high electric field (Figure 3c), does the electron injection happen<sup>63–65</sup> and reduction take place. Otherwise, direct tunneling (Figure 3d) through the ground state of the molecule occurs.

Combining all the results from theory and experiment, we propose (Figure 3e) an electron injection-induced redox switching mechanism in order to explain the single-molecule bistable conductance signature of the positively charged viologen during the elongation of the junction. The Au tip picks up a  $\text{BIPY-Me}^{2+}$  molecule at its terminal group through the electrostatic interaction between Au and the pyridinium- $\text{N}^+$ . The gap, which is below 0.5 nm with an extremely large electric field, will facilitate the electron injection from the Au tip to  $\text{BIPY-Me}^{2+}$ , creating a radical cationic  $\text{BIPY-Me}^{\bullet+}$  species in its HC state. When the junction keeps increasing and reaches 0.7 nm, the electric field decreases, leading to the loss of one electron from the SOMO of the  $\text{BIPY-Me}^{\bullet+}$  to the bottom Au electrode, i.e., the  $\text{BIPY-Me}^{\bullet+}$  is oxidized to its dicationic ground state of  $\text{BIPY-Me}^{2+}$  in its LC state before the

rupture of the junction occurs. This process cannot happen in  $\text{BIPY}$  because it is not a redox-active compound (Figure S25).

We note that the injection/extraction of electrons is essential for the redox switching mechanism and is related to the barrier provided by the substituents on the pyridinium- $\text{N}$ . As a result, we prepared (Figure 2l, inset) four more viologens with different substituents of increasing size, namely, ethyl, *n*-propyl, *i*-propyl, and adamantyl. Conductance studies show (Figure 2l and Figure S32) that only  $\text{BIPY-Et}^{2+}$  with ethyl substituents maintains the binary conductance feature characteristic of  $\text{BIPY-Me}^{2+}$ . Since larger substituents, namely, *n*-propyl, *i*-propyl, and adamantyl, form higher barriers, electrons cannot be injected effectively. It follows that we only obtain (Figure 2i, blue line) direct tunneling currents in the case of  $\text{BIPY-nPr}^{2+}$ ,  $\text{BIPY-iPr}^{2+}$ ,  $\text{BIPY-Ada}^{2+}$ . This distinction supports the electron injection-induced redox switching mechanism in the case of  $\text{BIPY-Me}^{2+}$  and  $\text{BIPY-Et}^{2+}$ . It also rules out the possibility that the HC state only comes from the molecule-electrode contact geometry when the molecules are lying on the Au substrate.

**System Expansion.** Next, we compared (Figure 4a) the length dependence of two series of molecules, namely, one based on the  $\text{Ex}^n\text{BIPY}$  ( $n = 0-3$ ) family with pyridine-terminated dative anchors and the other one based on the  $\text{Ex}^n\text{BIPY-Me} \cdot 2\text{PF}_6$  ( $n = 0-3$ ) family with pyridinium-terminated electrostatic anchors, by extracting (Figures S33–S35) the conductance values from the 1D and 2D histogram peak values and then plotting them against the length of the molecules on a semilog scale. We find (Figure 4a) that the conductance trends for both families are nearly linear on the plot, indicating that the conductance depends<sup>66</sup> exponentially on length according to the relationship

$$G = G_c \exp(-\beta L) \quad (1)$$

where  $G$  is the conductance,  $G_c$  is the contact conductance arising from the molecule-electrode contact,  $L$  is the length of the molecule, and  $\beta$  is the decay constant that depends on the tunneling barrier associated with the single-molecule junction. Using eq 1, we determined (Figure 4a, red dots and lines) a decay constant for  $\text{Ex}^n\text{BIPY}$  of  $\beta = 2.91$   $\text{nm}^{-1}$ , a value which is comparable with those recorded<sup>14,22,46</sup> in previous reports. By contrast, the conductance of pyridinium-terminated  $\text{Ex}^n\text{BIPY-Me} \cdot 2\text{PF}_6$  shows (Figure 4a, blue dots and lines) a slightly smaller decay constant of  $2.29$   $\text{nm}^{-1}$ , indicating that electrostatic anchors form robust contacts with Au electrodes and enable stable measurements to be made of conductances.

The counterion effect was also examined (Figure 4b) by exchanging the  $\text{PF}_6^-$  with  $\text{BF}_4^-$  and  $\text{SbF}_6^-$ .  $\text{BIPY-Me}^{2+}$  with all three of these counterions dissolves easily in MeCN. Other anions, for example, halide counterions, are not suitable candidates since their salts are almost insoluble in MeCN. The choice of solvent has to remain constant in all the experiments since the influence of solvent effects<sup>67,68</sup> on single-molecule conductances cannot be ruled out. By extracting (Figure S36) the conductance values from the 1D and 2D histogram peaks, we obtained (Figure 4b) a binary conductance feature in the case of all three compounds, namely,  $\text{BIPY-Me} \cdot 2\text{BF}_4$ ,  $\text{BIPY-Me} \cdot 2\text{PF}_6$ ,  $\text{BIPY-Me} \cdot 2\text{SbF}_6$ , with their LC states centered on  $\sim 10^{-4.0}$   $G_0$ , while their HC states are distributed across a broader range between  $10^{-2.0}$  to  $10^{-3.0}$   $G_0$ . This observation indicates that the radical metastable state is more sensitive to counterion exchange than the dicationic ground state.

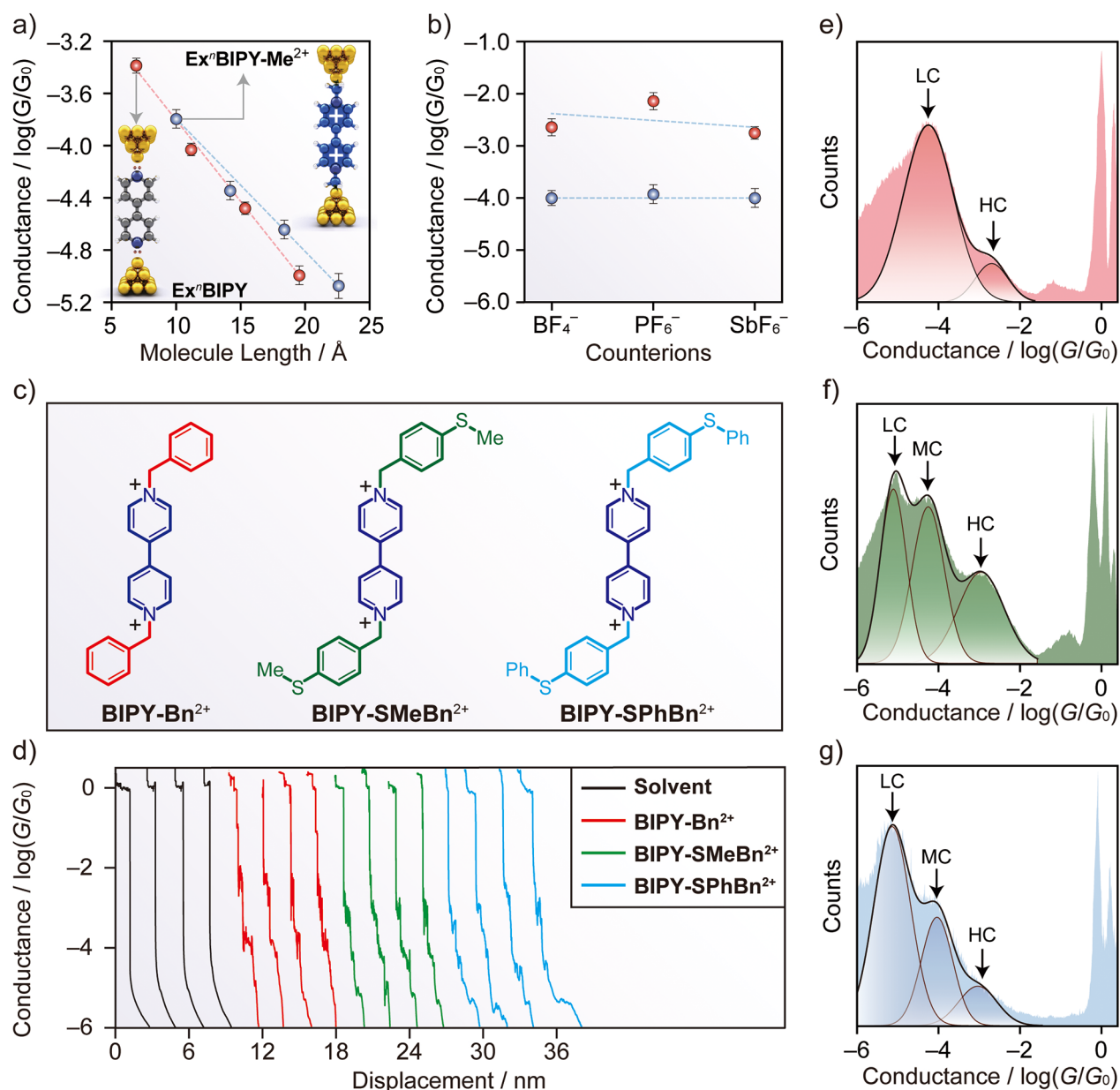


**Figure 4.** Applying pyridinium electrostatic anchors to other backbones. (a) Conductance determined from Gaussian fits to 1D histogram peaks for the  $\text{Ex}^n\text{BIPY}$  (red) and  $\text{Ex}^n\text{BIPY-Me-2PF}_6$  (blue) ( $n = 0-3$ ) families as a function of the molecular length. The dashed lines show an exponential fit to the data points. (b) Conductance determined from Gaussian fits to 1D histogram peaks of  $\text{BIPY-Me}^{2+}$  with different counterions. (c) Structural formulas of  $\text{BIPY-Bn-2PF}_6$ ,  $\text{BIPY-SMeBn-2PF}_6$ , and  $\text{BIPY-SPhBn-2PF}_6$  terminated by benzyl, methyl sulfide benzyl, and phenyl sulfide benzyl, respectively. (d) Typical individual conductance–displacement traces recorded in break junction measurements. 1D conductance histograms for  $\text{BIPY-Bn-2PF}_6$  (e),  $\text{BIPY-SMeBn-2PF}_6$  (f), and  $\text{BIPY-SPhBn-2PF}_6$  (g), showing multilevel conductance signatures.

Finally, in order to compare the competitive relationship between electrostatic anchors and other anchors when they are present in the same molecule, we prepared (Figure 4c) three benzyl derivatives, namely,  $\text{BIPY-Bn-2PF}_6$ ,  $\text{BIPY-SMeBn-2PF}_6$ , and  $\text{BIPY-SPhBn-2PF}_6$ , and measured (Figure 4d) their conductances. In the case of the  $\text{BIPY-Bn}^{2+}$  junction, since the benzyl substituents stabilize the radical, we observed (Figure 4e and Figure S37a) two-level conductance states, namely, a HC radical state at  $10^{-2.6} G_0$  and a LC dicationic state at  $10^{-4.2} G_0$ , regardless of the steric bulk size of the end group. In the case of the  $\text{BIPY-SMeBn}^{2+}$  junction, however, we observed (Figure 4f and Figure S37d) three conductance states, namely, an HC, a middle-conductance (MC), and an

LC state centered on  $\sim 10^{-2.9}$ ,  $\sim 10^{-4.2}$ , and  $\sim 10^{-5.1} G_0$ , respectively. The MC and HC states of  $\text{BIPY-SMeBn}^{2+}$  are close to the values for the LC and HC states of  $\text{BIPY-Bn}^{2+}$ . Furthermore, considering the similar displacement of these two pairs of states in the 2D histograms (Figure S37), the MC and HC states of  $\text{BIPY-SMeBn}^{2+}$  can be ascribed, respectively, to the dicationic ground state and a metastable radical state. The LC state of  $\text{BIPY-SMeBn}^{2+}$ , with its much lower conductance and longer displacement, is the result of the tunneling through S-to-S connections. These observations are confirmed in the case of the  $\text{BIPY-SPhBn}^{2+}$  junction. A three-level conductance feature similar to that for  $\text{BIPY-SMeBn}^{2+}$  was observed (Figure 4g and Figure S37f). We note that in comparison

with methyl substituents on S, phenyl substituents on S help to form a stronger binding between the S and Au atoms. Thus, in the BIPY-SPhBn<sup>2+</sup> junction, the percentage of the LC state increases, while the HC state decreases simultaneously.

## CONCLUSION

In this research, we have investigated the charge transport properties of a series of positively charged pyridinium-anchored compounds with different substituents and backbones. Using a combination of ensemble experiments and single-molecule measurements, we have demonstrated that the pyridinium units serve as stable anchors facilitating connections between the molecules and Au electrodes. Our results show that the charge transport in pyridinium-anchored oligophenylenes exhibits a quantum tunneling mechanism. In addition, we observe binary switching states, namely, a cationic ground state and a radical cationic metastable state, in the case of the dimethyl viologen junction. These results reveal the role of anchors in controlling redox reactions. Anchors facilitate an increased understanding of conductance in junctions involving molecules with complex structures. This research will aid in the design and development of new chemistry as it relates to molecular electronics.

## ASSOCIATED CONTENT

### Supporting Information

The Supporting Information is available free of charge at <https://pubs.acs.org/doi/10.1021/jacs.0c12664>.

Detailed synthetic procedures and characterization data (NMR spectroscopy) for all the compounds (PDF)

Cartesian coordinates (PDF)

## AUTHOR INFORMATION

### Corresponding Author

J. Fraser Stoddart – Department of Chemistry, Northwestern University, Evanston, Illinois 60208, United States; School of Chemistry, University of New South Wales, Sydney, NSW 2052, Australia; Stoddart Institute of Molecular Science, Department of Chemistry, Zhejiang University, Hangzhou 310021, China; ZJU-Hangzhou Global Scientific and Technological Innovation Center, Hangzhou 311215, China; [orcid.org/0000-0003-3161-3697](https://orcid.org/0000-0003-3161-3697); Email: [stoddart@northwestern.edu](mailto:stoddart@northwestern.edu)

### Authors

Hongliang Chen – Department of Chemistry, Northwestern University, Evanston, Illinois 60208, United States; [orcid.org/0000-0002-4442-7984](https://orcid.org/0000-0002-4442-7984)

Vitor Brasiliense – Department of Chemistry, Northwestern University, Evanston, Illinois 60208, United States; Université Paris-Saclay, ENS Paris-Saclay, CNRS, PPSM, 91190 Gif/Yvette, France; [orcid.org/0000-0002-5515-2218](https://orcid.org/0000-0002-5515-2218)

Jingshan Mo – State Key Laboratory of Optoelectronic Materials and Technologies, School of Electronics and Information Technology, Sun Yat-Sen University, Guangzhou 510006, China; [orcid.org/0000-0003-2844-6314](https://orcid.org/0000-0003-2844-6314)

Long Zhang – Department of Chemistry, Northwestern University, Evanston, Illinois 60208, United States; [orcid.org/0000-0002-4631-158X](https://orcid.org/0000-0002-4631-158X)

Yang Jiao – Department of Chemistry, Northwestern University, Evanston, Illinois 60208, United States; [orcid.org/0000-0002-8437-0038](https://orcid.org/0000-0002-8437-0038)

Zhu Chen – Department of Chemistry, Northwestern University, Evanston, Illinois 60208, United States; [orcid.org/0000-0001-5889-5415](https://orcid.org/0000-0001-5889-5415)

Leighton O. Jones – Department of Chemistry, Northwestern University, Evanston, Illinois 60208, United States; [orcid.org/0000-0001-6657-2632](https://orcid.org/0000-0001-6657-2632)

Gen He – State Key Laboratory of Optoelectronic Materials and Technologies, School of Electronics and Information Technology, Sun Yat-Sen University, Guangzhou 510006, China; [orcid.org/0000-0003-1394-0053](https://orcid.org/0000-0003-1394-0053)

Qing-Hui Guo – Department of Chemistry, Northwestern University, Evanston, Illinois 60208, United States; [orcid.org/0000-0002-9946-0810](https://orcid.org/0000-0002-9946-0810)

Xiao-Yang Chen – Department of Chemistry, Northwestern University, Evanston, Illinois 60208, United States; [orcid.org/0000-0003-3449-4136](https://orcid.org/0000-0003-3449-4136)

Bo Song – Department of Chemistry, Northwestern University, Evanston, Illinois 60208, United States; [orcid.org/0000-0002-4337-848X](https://orcid.org/0000-0002-4337-848X)

George C. Schatz – Department of Chemistry, Northwestern University, Evanston, Illinois 60208, United States; [orcid.org/0000-0001-5837-4740](https://orcid.org/0000-0001-5837-4740)

Complete contact information is available at: <https://pubs.acs.org/doi/10.1021/jacs.0c12664>

### Author Contributions

<sup>S</sup>H.C. and V.B. contributed equally.

### Notes

The authors declare no competing financial interest.

## ACKNOWLEDGMENTS

We thank Northwestern University for its continued support of this research. This work made use of the IMSERC NMR facility at Northwestern University, which has received support from the Soft and Hybrid Nanotechnology Experimental (SHyNE) Resource (NSF ECCS-2025633) and Northwestern University. This work made use of the Keck-II XPS facility of Northwestern University's NUANCE Center, which has received support from the SHyNE Resource, the IIN, and Northwestern's MRSEC program (NSF DMR-1720139). L.O.J. and G.C.S. acknowledge support from the Department of Energy, Office of Basic Energy Science, under grant DE-SC0004752. This research was also supported in part through the computational resources and staff contributions provided by the Quest high performance computing facility at Northwestern University which is jointly supported by the Office of the Provost, the Office for Research, and Northwestern University Information Technology. We thank Prof. W. Hong for help with the STM-BJ setup.

## REFERENCES

- (1) Aviram, A.; Ratner, M. A. Molecular Rectifiers. *Chem. Phys. Lett.* **1974**, *29*, 277–283.
- (2) Joachim, C.; Gimzewski, J. K.; Aviram, A. Electronics Using Hybrid-Molecular and Mono-Molecular Devices. *Nature* **2000**, *408*, 541–548.
- (3) Flood, A. H.; Stoddart, J. F.; Steuerman, D. W.; Heath, J. R. Whence Molecular Electronics? *Science* **2004**, *306*, 2055–2056.

- (4) Joachim, C.; Ratner, M. A. Molecular Electronics: Some Views on Transport Junctions and Beyond. *Proc. Natl. Acad. Sci. U. S. A.* **2005**, *102*, 8801–8808.
- (5) Ratner, M. A. Brief History of Molecular Electronics. *Nat. Nanotechnol.* **2013**, *8*, 378–381.
- (6) Lambert, C. J. Basic Concepts of Quantum Interference and Electron Transport in Single-Molecule Electronics. *Chem. Soc. Rev.* **2015**, *44*, 875–888.
- (7) Xiang, D.; Wang, X. L.; Jia, C. C.; Lee, T.; Guo, X. F. Molecular-Scale Electronics: From Concept to Function. *Chem. Rev.* **2016**, *116*, 4318–4440.
- (8) Su, T. A.; Neupane, M.; Steigerwald, M. L.; Venkataraman, L.; Nuckolls, C. Chemical Principles of Single-Molecule Electronics. *Nat. Rev. Mater.* **2016**, *1*, 16002.
- (9) Xin, N.; Guan, J.; Zhou, C.; Chen, X.; Gu, C.; Li, Y.; Ratner, M. A.; Nitzan, A.; Stoddart, J. F.; Guo, X. Concepts in the Design and Engineering of Single-Molecule Electronic Devices. *Nat. Rev. Phys.* **2019**, *1*, 211–230.
- (10) Gehring, P.; Thijssen, J. M.; van der Zant, H. S. J. Single-Molecule Quantum-Transport Phenomena in Break Junctions. *Nat. Rev. Phys.* **2019**, *1*, 381–396.
- (11) Zhang, J. L.; Zhong, J. Q.; Lin, J. D.; Hu, W. P.; Wu, K.; Xu, G. Q.; Wee, A. T. S.; Chen, W. Towards Single Molecule Switches. *Chem. Soc. Rev.* **2015**, *44*, 2998–3022.
- (12) Jia, C.; Guo, X. Molecule-Electrode Interfaces in Molecular Electronic Devices. *Chem. Soc. Rev.* **2013**, *42*, 5642–5660.
- (13) Venkataraman, L.; Klare, J. E.; Tam, I. W.; Nuckolls, C.; Hybertsen, M. S.; Steigerwald, M. L. Single-Molecule Circuits with Well-Defined Molecular Conductance. *Nano Lett.* **2006**, *6*, 458–462.
- (14) Kamenetska, M.; Quek, S. Y.; Whalley, A. C.; Steigerwald, M. L.; Choi, H. J.; Louie, S. G.; Nuckolls, C.; Hybertsen, M. S.; Neaton, J. B.; Venkataraman, L. Conductance and Geometry of Pyridine-Linked Single-Molecule Junctions. *J. Am. Chem. Soc.* **2010**, *132*, 6817–6821.
- (15) Kim, T.; Darancet, P.; Widawsky, J. R.; Kotiuga, M.; Quek, S. Y.; Neaton, J. B.; Venkataraman, L. Determination of Energy Level Alignment and Coupling Strength in 4,4'-Bipyridine Single-Molecule Junctions. *Nano Lett.* **2014**, *14*, 794–798.
- (16) Mishchenko, A.; Zotti, L. A.; Vonlanthen, D.; Bürkle, M.; Pauly, F.; Cuevas, J. C.; Mayor, M.; Wandlowski, T. Single-Molecule Junctions Based on Nitrile-Terminated Biphenyls: A Promising New Anchoring Group. *J. Am. Chem. Soc.* **2011**, *133*, 184–187.
- (17) Kim; Beebe, J. M.; Jun, Y.; Zhu, X.-Y.; Frisbie, C. D. Correlation between HOMO Alignment and Contact Resistance in Molecular Junctions: Aromatic Thiols versus Aromatic Isocyanides. *J. Am. Chem. Soc.* **2006**, *128*, 4970–4971.
- (18) Ko, C.-H.; Huang, M.-J.; Fu, M.-D.; Chen, C.-h. Superior Contact for Single-Molecule Conductance: Electronic Coupling of Thiolate and Isothiocyanate on Pt, Pd, and Au. *J. Am. Chem. Soc.* **2010**, *132*, 756–764.
- (19) Garner, M. H.; Li, H.; Chen, Y.; Su, T. A.; Shangguan, Z.; Paley, D. W.; Liu, T.; Ng, F.; Li, H.; Xiao, S.; Nuckolls, C.; Venkataraman, L.; Solomon, G. C. Comprehensive Suppression of Single-Molecule Conductance Using Destructive  $\sigma$ -Interference. *Nature* **2018**, *558*, 415–419.
- (20) Kamenetska, M.; Koentopp, M.; Whalley, A. C.; Park, Y. S.; Steigerwald, M. L.; Nuckolls, C.; Hybertsen, M. S.; Venkataraman, L. Formation and Evolution of Single-Molecule Junctions. *Phys. Rev. Lett.* **2009**, *102*, 126803.
- (21) Zotti, L. A.; Kirchner, T.; Cuevas, J.-C.; Pauly, F.; Huhn, T.; Scheer, E.; Erbe, A. Revealing the Role of Anchoring Groups in the Electrical Conduction Through Single-Molecule Junctions. *Small* **2010**, *6*, 1529–1535.
- (22) Li, S.; Yu, H.; Schwieter, K.; Chen, K.; Li, B.; Liu, Y.; Moore, J. S.; Schroeder, C. M. Charge Transport and Quantum Interference Effects in Oxazole-Terminated Conjugated Oligomers. *J. Am. Chem. Soc.* **2019**, *141*, 16079–16084.
- (23) Prins, F.; Barreiro, A.; Ruitenber, J. W.; Seldenthuis, J. S.; Aliaga-Alcalde, N.; Vandersypen, L. M. K.; van der Zant, H. S. J. Room-Temperature Gating of Molecular Junctions Using Few-Layer Graphene Nanogap Electrodes. *Nano Lett.* **2011**, *11*, 4607–4611.
- (24) Ullmann, K.; Coto, P. B.; Leitherer, S.; Molina-Ontoria, A.; Martín, N.; Thoss, M.; Weber, H. B. Single-Molecule Junctions with Epitaxial Graphene Nanoelectrodes. *Nano Lett.* **2015**, *15*, 3512–3518.
- (25) Lau, C. S.; Sadeghi, H.; Rogers, G.; Sangtarash, S.; Dallas, P.; Porfyraakis, K.; Warner, J.; Lambert, C. J.; Briggs, G. A. D.; Mol, J. A. Redox-Dependent Franck-Condon Blockade and Avalanche Transport in a Graphene-Fullerene Single-Molecule Transistor. *Nano Lett.* **2016**, *16*, 170–176.
- (26) Burzurí, E.; García-Fuente, A.; García-Suárez, V.; Senthil Kumar, K.; Ruben, M.; Ferrer, J.; van der Zant, H. S. J. Spin-State Dependent Conductance Switching in Single Molecule-Graphene Junctions. *Nanoscale* **2018**, *10*, 7905–7911.
- (27) Chen, F.; Li, X.; Hihath, J.; Huang, Z.; Tao, N. Effect of Anchoring Groups on Single-Molecule Conductance: Comparative Study of Thiol-, Amine-, and Carboxylic-Acid-Terminated Molecules. *J. Am. Chem. Soc.* **2006**, *128*, 15874–15881.
- (28) Hong, W.; Li, H.; Liu, S.-X.; Fu, Y.; Li, J.; Kaliginedi, V.; Decurtins, S.; Wandlowski, T. Trimethylsilyl-Terminated Oligo-(phenylene ethynylene)s: An Approach to Single-Molecule Junctions with Covalent Au–C  $\sigma$ -Bonds. *J. Am. Chem. Soc.* **2012**, *134*, 19425–19431.
- (29) Hines, T.; Díez-Pérez, I.; Nakamura, H.; Shimazaki, T.; Asai, Y.; Tao, N. Controlling Formation of Single-Molecule Junctions by Electrochemical Reduction of Diazonium Terminal Groups. *J. Am. Chem. Soc.* **2013**, *135*, 3319–3322.
- (30) Batra, A.; Kladnik, G.; Gorjizadeh, N.; Meisner, J.; Steigerwald, M.; Nuckolls, C.; Quek, S. Y.; Cvetko, D.; Morgante, A.; Venkataraman, L. Trimethyltin-Mediated Covalent Gold–Carbon Bond Formation. *J. Am. Chem. Soc.* **2014**, *136*, 12556–12559.
- (31) Li, S.; Yu, H.; Chen, X.; Gewirth, A. A.; Moore, J. S.; Schroeder, C. M. Covalent Ag–C Bonding Contacts from Unprotected Terminal Acetylens for Molecular Junctions. *Nano Lett.* **2020**, *20*, 5490–5495.
- (32) Guo, X.; Small, J. P.; Klare, J. E.; Wang, Y.; Purewal, M. S.; Tam, I. W.; Hong, B. H.; Caldwell, R.; Huang, L.; O'Brien, S.; Yan, J.; Breslow, R.; Wind, S. J.; Hone, J.; Kim, P.; Nuckolls, C. Covalently Bridging Gaps in Single-Walled Carbon Nanotubes with Conducting Molecules. *Science* **2006**, *311*, 356–359.
- (33) Cao, Y.; Dong, S.; Liu, S.; He, L.; Gan, L.; Yu, X.; Steigerwald, M. L.; Wu, X.; Liu, Z.; Guo, X. Building High-Throughput Molecular Junctions Using Indented Graphene Point Contacts. *Angew. Chem., Int. Ed.* **2012**, *51*, 12228–12232.
- (34) Jia, C.; Migliore, A.; Xin, N.; Huang, S.; Wang, J.; Yang, Q.; Wang, S.; Chen, H.; Wang, D.; Feng, B.; Liu, Z.; Zhang, G.; Qu, D.-H.; Tian, H.; Ratner, M. A.; Xu, H. Q.; Nitzan, A.; Guo, X. Covalently Bonded Single-Molecule Junctions with Stable and Reversible Photoswitched Conductivity. *Science* **2016**, *352*, 1443–1445.
- (35) Wang, H.; Wang, Z. X.; Wang, Y.; Hihath, J.; Chen, H. Y.; Li, Y. Q.; Tao, N. J. Potential Dependence of Mechanical Stability and Electronic Coupling of Single S-Au Bonds. *J. Am. Chem. Soc.* **2018**, *140*, 18074–18081.
- (36) Inkpen, M. S.; Liu, Z. F.; Li, H. X.; Campos, L. M.; Neaton, J. B.; Venkataraman, L. Non-Chemisorbed Gold-Sulfur Binding Prevails in Self-Assembled Monolayers. *Nat. Chem.* **2019**, *11*, 351–358.
- (37) Bejarano, F.; Olavarria-Contreras, I. J.; Droghetti, A.; Rungger, I.; Rudnev, A.; Gutierrez, D.; Mas-Torrent, M.; Veciana, J.; van der Zant, H. S. J.; Rovira, C.; Burzurí, E.; Crivillers, N. Robust Organic Radical Molecular Junctions Using Acetylene Terminated Groups for C–Au Bond Formation. *J. Am. Chem. Soc.* **2018**, *140*, 1691–1696.
- (38) Batra, A.; Darancet, P.; Chen, Q. S.; Meisner, J. S.; Widawsky, J. R.; Neaton, J. B.; Nuckolls, C.; Venkataraman, L. Tuning Rectification in Single-Molecular Diodes. *Nano Lett.* **2013**, *13*, 6233–6237.
- (39) Lampert, Z. A.; Broadnax, A. D.; Scharmann, B.; Bradford, R. W.; DelaCourt, A.; Meyer, N.; Li, H.; Geyer, S. M.; Thonhauser, T.; Welker, M. E.; Jurchescu, O. D. Molecular Rectifiers on Silicon: High Performance by Enhancing Top-Electrode/Molecule Coupling. *ACS Appl. Mater. Interfaces* **2019**, *11*, 18564–18570.

- (40) Nguyen, Q. v.; Martin, P.; Frath, D.; Della Rocca, M. L.; Lafolet, F.; Barraud, C.; Lafarge, P.; Mukundan, V.; James, D.; McCreery, R. L.; Lacroix, J.-C. Control of Rectification in Molecular Junctions: Contact Effects and Molecular Signature. *J. Am. Chem. Soc.* **2017**, *139*, 11913–11922.
- (41) Wang, X.; Zhi, L. J.; Müllen, K. Transparent, Conductive Graphene Electrodes for Dye-Sensitized Solar Cells. *Nano Lett.* **2008**, *8*, 323–327.
- (42) Herrero, I. L.; Ismael, A. K.; Milan, D. C.; Vezzoli, A.; Martin, S.; Gonzalez-Orive, A.; Grace, I.; Lambert, C.; Serrano, J. L.; Nichols, R. J.; Cea, P. Unconventional Single-Molecule Conductance Behavior for a New Heterocyclic Anchoring Group: Pyrazolyl. *J. Phys. Chem. Lett.* **2018**, *9*, 5364–5372.
- (43) Tang, C.; Zheng, J.; Ye, Y.; Liu, J.; Chen, L.; Yan, Z.; Chen, Z.; Chen, L.; Huang, X.; Bai, J.; Chen, Z.; Shi, J.; Xia, H.; Hong, W. Electric-Field-Induced Connectivity Switching in Single-Molecule Junctions. *iScience* **2020**, *23*, 100770.
- (44) Pan, X. Y.; Lawson, B.; Rustad, A. M.; Kamenetska, M. pH-Activated Single Molecule Conductance and Binding Mechanism of Imidazole on Gold. *Nano Lett.* **2020**, *20*, 4687–4692.
- (45) Xu, B.; Tao, N. J. Measurement of Single-Molecule Resistance by Repeated Formation of Molecular Junctions. *Science* **2003**, *301*, 1221–1223.
- (46) Venkataraman, L.; Klare, J. E.; Nuckolls, C.; Hybertsen, M. S.; Steigerwald, M. L. Dependence of Single-Molecule Junction Conductance on Molecular Conformation. *Nature* **2006**, *442*, 904–907.
- (47) Osorio, H. M.; Martín, S.; Milan, D. C.; González-Orive, A.; Gluyas, J. B. G.; Higgins, S. J.; Low, P. J.; Nichols, R. J.; Cea, P. Influence of Surface Coverage on the Formation of 4,4'-Bipyridinium (Viologen) Single Molecular Junctions. *J. Mater. Chem. C* **2017**, *5*, 11717–11723.
- (48) Chen, H.; Zheng, H.; Hu, C.; Cai, K.; Jiao, Y.; Zhang, L.; Jiang, F.; Roy, I.; Qiu, Y.; Shen, D.; Feng, Y.; Alsubaie, F. M.; Guo, H.; Hong, W.; Stoddart, J. F. Giant Conductance Enhancement of Intramolecular Circuits through Interchannel Gating. *Matter* **2020**, *2*, 378–389.
- (49) Chen, H.; Dong, S.; Bai, M.; Cheng, N.; Wang, H.; Li, M.; Du, H.; Hu, S.; Yang, Y.; Yang, T.; Zhang, F.; Gu, L.; Meng, S.; Hou, S.; Guo, X. Solution-Processable, Low-Voltage, and High-Performance Monolayer Field-Effect Transistors with Aqueous Stability and High Sensitivity. *Adv. Mater.* **2015**, *27*, 2113–2120.
- (50) Qi, Y.; Brasiliense, V.; Ueltschi, T. W.; Park, J. E.; Wasielewski, M. R.; Schatz, G. C.; Van Duyne, R. P. Plasmon-Driven Chemistry in Ferri-/Ferrocyanide Gold Nanoparticle Oligomers: A SERS Study. *J. Am. Chem. Soc.* **2020**, *142*, 13120–13129.
- (51) Chen, Z.; Jiang, S.; Kang, G.; Nguyen, D.; Schatz, G. C.; Van Duyne, R. P. Operando Characterization of Iron Phthalocyanine Deactivation during Oxygen Reduction Reaction Using Electrochemical Tip-Enhanced Raman Spectroscopy. *J. Am. Chem. Soc.* **2019**, *141*, 15684–15692.
- (52) Jones, L. O.; Mosquera, M. A.; Schatz, G. C.; Ratner, M. A. Molecular Junctions Inspired by Nature: Electrical Conduction through Noncovalent Nanobelts. *J. Phys. Chem. B* **2019**, *123*, 8096–8102.
- (53) Jones, L. O.; Mosquera, M. A.; Ratner, M. A.; Schatz, G. C. Orbital Control and Coherent Charge Transport in Transition Metal Platinum(II)–Platinum(II) Lantern Complexes in Molecular Junctions. *J. Phys. Chem. C* **2020**, *124*, 3233–3241.
- (54) Quek, S. Y.; Kamenetska, M.; Steigerwald, M. L.; Choi, H. J.; Louie, S. G.; Hybertsen, M. S.; Neaton, J. B.; Venkataraman, L. Mechanically Controlled Binary Conductance Switching of a Single-Molecule Junction. *Nat. Nanotechnol.* **2009**, *4*, 230–234.
- (55) Kamenetska, M.; Quek, S. Y.; Whalley, A. C.; Steigerwald, M. L.; Choi, H. J.; Louie, S. G.; Nuckolls, C.; Hybertsen, M. S.; Neaton, J. B.; Venkataraman, L. Conductance and Geometry of Pyridine-Linked Single-Molecule Junctions. *J. Am. Chem. Soc.* **2010**, *132*, 6817–6821.
- (56) Huang, C.; Jevric, M.; Borges, A.; Olsen, S. T.; Hamill, J. M.; Zheng, J.-T.; Yang, Y.; Rudnev, A.; Baghernejad, M.; Broekmann, P.; Petersen, A. U.; Wandlowski, T.; Mikkelsen, K. V.; Solomon, G. C.; Brøndsted Nielsen, M.; Hong, W. Single-Molecule Detection of Dihydroazulene Photo-Thermal Reaction Using Break Junction Technique. *Nat. Commun.* **2017**, *8*, 15436.
- (57) Makk, P.; Tomaszewski, D.; Martinek, J.; Balogh, Z.; Csonka, S.; Wawrzyniak, M.; Frei, M.; Venkataraman, L.; Halbritter, A. Correlation Analysis of Atomic and Single-Molecule Junction Conductance. *ACS Nano* **2012**, *6*, 3411–3423.
- (58) Liu, J.; Zhao, X.; Al-Galiby, Q.; Huang, X.; Zheng, J.; Li, R.; Huang, C.; Yang, Y.; Shi, J.; Manrique, D. Z.; Lambert, C. J.; Bryce, M. R.; Hong, W. Radical-Enhanced Charge Transport in Single-Molecule Phenothiazine Electrical Junctions. *Angew. Chem., Int. Ed.* **2017**, *56*, 13061–13065.
- (59) Low, J. Z.; Kladnik, G.; Patera, L. L.; Sokolov, S.; Lovat, G.; Kumarasamy, E.; Repp, J.; Campos, L. M.; Cvetko, D.; Morgante, A.; Venkataraman, L. The Environment-Dependent Behavior of the Blatter Radical at the Metal–Molecule Interface. *Nano Lett.* **2019**, *19*, 2543–2548.
- (60) Devadas, M. S.; Kim, J.; Sinn, E.; Lee, D.; Goodson, T.; Ramakrishna, G. Unique Ultrafast Visible Luminescence in Monolayer-Protected Au<sub>25</sub> Clusters. *J. Phys. Chem. C* **2010**, *114*, 22417–22423.
- (61) Stamplecoskie, K. G.; Chen, Y.-S.; Kamat, P. V. Excited-State Behavior of Luminescent Glutathione-Protected Gold Clusters. *J. Phys. Chem. C* **2014**, *118*, 1370–1376.
- (62) Stamplecoskie, K. G.; Kamat, P. V. Size-Dependent Excited State Behavior of Glutathione-Capped Gold Clusters and Their Light-Harvesting Capacity. *J. Am. Chem. Soc.* **2014**, *136*, 11093–11099.
- (63) Yang, W.; Vlachopoulos, N.; Boschloo, G. Impact of Local Electric Fields on Charge-Transfer Processes at the TiO<sub>2</sub>/Dye/Electrolyte Interface. *ACS Energy Letters* **2017**, *2*, 161–167.
- (64) Wong, E. L.; Winchester, A. J.; Pareek, V.; Madéo, J.; Man, M. K. L.; Dani, K. M. Pulling Apart Photoexcited Electrons by Photoinducing an In-Plane Surface Electric Field. *Science Advances* **2018**, *4*, No. eaat9722.
- (65) Clark, M. L.; Ge, A.; Videla, P. E.; Rudshiteyn, B.; Miller, C. J.; Song, J.; Batista, V. S.; Lian, T.; Kubiak, C. P. CO<sub>2</sub> Reduction Catalysts on Gold Electrode Surfaces Influenced by Large Electric Fields. *J. Am. Chem. Soc.* **2018**, *140*, 17643–17655.
- (66) Xiang, L.; Hines, T.; Palma, J. L.; Lu, X.; Mujica, V.; Ratner, M. A.; Zhou, G.; Tao, N. Non-exponential Length Dependence of Conductance in Iodide-Terminated Oligothiophene Single-Molecule Tunneling Junctions. *J. Am. Chem. Soc.* **2016**, *138*, 679–687.
- (67) Milan, D. C.; Al-Owaedi, O. A.; Oerthel, M.-C.; Marqués-González, S.; Brooke, R. J.; Bryce, M. R.; Cea, P.; Ferrer, J.; Higgins, S. J.; Lambert, C. J.; Low, P. J.; Manrique, D. Z.; Martin, S.; Nichols, R. J.; Schwarzacher, W.; García-Suárez, V. M. Solvent Dependence of the Single Molecule Conductance of Oligoynne-Based Molecular Wires. *J. Phys. Chem. C* **2016**, *120*, 15666–15674.
- (68) Kastlunger, G.; Stadler, R. Charge Localization on a Redox-Active Single-Molecule Junction and Its Influence on Coherent Electron Transport. *Phys. Rev. B: Condens. Matter Mater. Phys.* **2013**, *88*, 035418.